Dynamic response of a compressible binary fluid mixture

Julien Lombard [1,*] I. Pagonabarraga [2,3,4] and E. Corvera Poiré [1,4,†]

[1] *Departamento de Física y Química Teórica, Facultad de Química, Universidad Nacional Autónoma de México, Mexico City 04510, Mexico*

[2] *Departament de Física de la Matèria Condensada, Universitat de Barcelona, Martí i Franquès 1, Barcelona 08028, Spain*

[3] *CECAM Centre Européen de Calcul Atomique et Moléculaire, École Polytechnique Fédérale de Lausanne (EPFL), Batochime, Avenue Forel 2, Lausanne CH-1015, Switzerland,*

[4] *UBICS Institute of Complex Systems, Universitat de Barcelona, Martí i Franquès 1, Barcelona 08028, Spain*

(Received 25 September 2019; accepted 28 April 2020; published 1 June 2020)

Binary fluids are present in a wide variety of systems at microscales, such as microfluidic devices containing drops, fluids with air bubbles trapped in them, and devices designed to mix fluids or to make two fluid substances react. Microfluidics devices are often, intentionally or unintentionally, subject to pulsatile forces due to the passing of drops. We demonstrate that when a binary fluid is subject to a pulsatile forcing, the compressibility of the lower viscosity phase is so important that it is able to generate resonances in the dynamic permeability of the whole system. This implies that the flow amplitude of a binary-fluid system in a zero-mean flow could be optimized at certain frequencies. The dynamic permeability is a powerful concept to describe the dynamics of the system, in the regime where the flow and the pressure gradient are related linearly in the frequency domain. We find two regimes for the frequency at which the resonance occurs: one dominated by a characteristic frequency of the system, related to the compressibility of the lower viscosity phase; and another one dominated by a more complex frequency, involving both the characteristic viscous frequency of the lower viscosity phase and a characteristic frequency related to the compressibility. In order to guide potential experiments, we calculate relevant quantities for two sets of binary fluids in standard microfluidic setups. Our calculations imply that for systems of typical microfluidic dimensions, involving a compressible fluid, the existence of the compressibility-induced resonance has to be contemplated for a correct description of the dynamics.

DOI: 10.1103/PhysRevFluids.5.064201

I. INTRODUCTION

The ability to control the flow of immiscible fluids in channels at micrometer scales is of fundamental importance for a wide range of applications in biological, medical sciences, physics, engineering and chemistry [1–6]. In particular, the use of a continuous flow of droplets or slug arrays has received increasing attention due to the precise control of chemical and biochemical reactions that they allow for. In such arrays, each slug behaves as an individual reaction chamber of submicron volume, independent from the other slugs [7–10]. One of the main advantages of this method over continuous two-phase bulk flow is to reduce the dispersion of the reagents over the channel length, since each section of the microchannel corresponds to a specific moment of the

*Author to whom correspondence should be addressed: juli1.lombard@gmail.com

†Author to whom correspondence should be addressed: eugenia.corvera@gmail.com

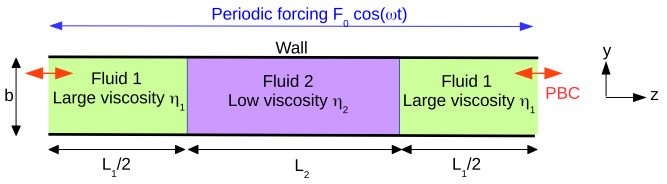

FIG. 1. Sketch of the system simulated: An immiscible binary fluid, displaying a viscosity contrast $\Delta\eta = (\eta_1 - \eta_2)/(\eta_1 + \eta_2)$ (with $\eta_2 < \eta_1$) in a Hele-Shaw cell is driven by a periodic forcing. The blue arrow represents the periodic forcing imposed over the whole fluid system. The red arrows at each extremity on the z axis show where the periodic boundary conditions (PBCs) are applied.

kinetic process [11,12]. However, even in slug-based reactions, the slow mixing between reagents is an issue, which is overcome by using specific channel geometries, such as winding channels or ribs [11,13]. Another way to achieve this purpose has emerged recently, which is the use of time pulsing or oscillatory flows, potentially coupled to a continuous flow [14–17].

Oscillatory flows in microfludics are also present intentionally or unintentionally in many microfluidics devices involving drops [18]. An efficient way to characterize the linear response of a fluid to a pulsatile pressure gradient is to use the dynamic permeability, a response function which quantifies the resistance to flow to each of the modes present in the pressure gradient. This function contains information about the fluid-confining media system, since it depends on fluid properties, channel geometry, elasticity, and the fluid interaction with the solid walls [19–24]. If the fluid [21] or the channel [22,25] exhibits an elastic behavior, the system dynamics can be profoundly modified.

While the dynamics of a Newtonian fluid flowing in one direction in rigid microchannels can be described analytically by solving the Navier-Stokes equations with a limited number of assumptions, the case of an immiscible binary fluid presents a higher level of complexity, due to the interplay between the two fluids and the interface.

In this paper, we study the pulsatile dynamics of a binary Newtonian compressible fluid in a rectangular microchannel, a situation that is relevant in many microfluidic devices involving drops [26], bubbly liquids [26–28], or bubbles [29,30]. We show that, in a regime where the compressibility of the fluids is irrelevant, often encountered in systems of drops, the framework of the dynamic permeability, originally derived for a single Newtonian noncompressible fluid, still holds for a binary fluid, provided that we compute the dynamic permeability using effective physical parameters. In other words, we find a quasiuniversal curve for the dynamic permeability of binary fluids, of different compositions, provided that we use a volume weighted viscosity in the description. We then unveil the existence of a resonant behavior due to the compressibility of the less viscous fluid, which leads to a sharp increase of the flow amplitude, relative to the steady state. We find that, at resonance, the lowest viscosity fluid behaves almost as if the other fluid, and the interface, did not exist. The importance of our results is that they enable the optimization of the flow magnitude in a zero-mean-flow binary-fluid system.

For our study, we use the lattice-Boltzmann method as described in Ref. [31], which has proved to be efficient to describe the dynamics of two fluids [32–34] and of flows in porous media [35,36]. This method is coupled to a phase-field model, that allows us to implement the viscosity contrast between the two fluids. We study a wide range of channel characteristics and compute parameters of standard microfluidic devices in order to show that the effects that we find are relevant to actual microfluidic experiments.

II. MODEL

We study a system that consists of two immiscible fluids of different viscosities in a rectangular microchannel of thickness, b, that is driven by a single-mode periodic forcing, $\vec{F}(t) = F_0 \cos(\omega t)\hat{k}$, identical at each point of the system. Figure 1 shows a sketch of the system. The total length

occupied by the fluids is $L = L_1 + L_2$, where L_1 is the length occupied by the fluid of larger viscosity and L_2 the length occupied by the fluid of lower viscosity. We write the volume fraction of each fluid as $x_1 = L_1/L$ and $x_2 = L_2/L$.

The governing equations of the system, with local density ρ, local velocity $\vec{v}$, and local viscosity η, are the equations of continuity and momentum conservation, namely,

$$\frac{\partial \rho}{\partial t} + \vec{\nabla} \cdot (\rho \vec{v}) = 0, \tag{1}$$

$$\rho\left(\frac{\partial \vec{v}}{\partial t} + (\vec{v} \cdot \vec{\nabla})\vec{v}\right) = -\vec{\nabla}\Pi - \vec{\nabla}P_\rho + \eta\nabla^2\vec{v} + \vec{F}(t). \tag{2}$$

In order to describe the binary mixture, these equations are coupled to a phase field model for an order parameter ϕ, which varies continuously from one phase to the other. Its dynamic equation is given by

$$\frac{\partial \phi}{\partial t} + (\vec{v} \cdot \vec{\nabla})\phi = M\nabla^2\mu. \tag{3}$$

The chemical potential μ and the tensor Π are functions of the local value of ϕ and its gradients. Their expressions are given in Eqs. (A3) and (A4) respectively. The term $\vec{\nabla}\Pi$ takes a nonzero value only at the interfaces, and accounts for the Young-Laplace pressure [37,38]. The term P_ρ in Eq. (2) accounts for compressibility effects. We consider that pressure is related to the local value of the density, through $P_\rho = c_s^2\rho$, where $c_s = 1/\sqrt{3}$ is the velocity of sound. The local viscosity in Eq. (2) depends on the order parameter as $\eta(\vec{r}) = \eta_1 + \frac{\phi(\vec{r})-\phi_1}{\phi_2-\phi_1}(\eta_2 - \eta_1)$ [39], that is, it depends on the phase at position, $\vec{r}$. With these considerations, we have a set of three coupled equations for $\rho(\vec{r}, t)$, $\vec{v}(\vec{r}, t)$, and $\phi(\vec{r}, t)$, given by Eqs. (1)–(3). Details of the lattice-Boltzmann method, as well as details of the coupling between the phase field model and the momentum conservation equation, are given in Appendix A.

As described in Appendix A, the model could consider different wetting interactions between the fluids and the wall. Here we choose to work with neutral wetting, that is, with wall properties such that there is no energetic preference of the wall for either of the fluids. This implies a contact angle of 90° between the fluid interface and the solid substrate. We also choose a large mobility ($M = 10$). In this way, the motion of the triple line at the wall follows closely the one of the interface at the center of the channel, minimizing the effect of the former on the latter [40–42]. This allows for the deformation of the interfaces, but limits the interpenetration of the two fluids [43]. We show in Supplemental Material a typical example of the deformation of the interfaces [44]. We set the surface tension to keep large capillary numbers Ca (ranging from 0.1 to 10), in order to reduce the capillary effect and keep the Laplace pressure negligible. Finally, we enforce a no-slip boundary condition for the velocity at the walls. We consider a simulation box of dimensions $X \times b \times L$ in the x, y, and z directions respectively, with $X = 3$. We fix periodic boundary conditions on the x and z directions, corresponding to a channel of width and length much larger than its thickness, b.

For the simulations presented in this paper, the magnitude F_0 of the driving force is low enough to avoid any turbulent behavior: the maximum Reynolds number in our simulations is $\mathrm{Re} = 1$. Also, since our forcing is oscillatory, during half of the cycle the less viscous fluid pushes the more viscous one. We could therefore expect all sorts of complex situations. All simulations are carried out in a regime of frequencies and forcing amplitudes where we observe periodic deformation of the interface, avoiding the development of instabilities.

III. CHARACTERIZATION OF THE BINARY FLUID DYNAMICS

For a single fluid of viscosity η, in a rigid channel, the generalized Darcy's law in the frequency domain, subject to an external periodic driving force $\hat{F}$, reads

$$\langle \hat{v}(z) \rangle = \frac{\hat{K}(\omega)}{\eta} \hat{F}, \tag{4}$$

where $\langle \hat{v}(z) \rangle$ is the fluid velocity, $\hat{v}_z(y, z)$, averaged over the microchannel height, $\hat{K}(\omega)$ is the dynamic permeability of the system, and ω is the frequency. Hats ($\hat{}$) denote quantities in the frequency domain. The analytical expression of $\hat{K}(\omega)$, for a single fluid of viscosity η and density ρ, between two parallel plates [45,46], is

$$\hat{K}(\omega) = -\frac{\eta}{i\omega\rho} \left[1 - \frac{\tan\left(\frac{b}{2}\sqrt{\frac{i\omega\rho}{\eta}}\right)}{\frac{b}{2}\sqrt{\frac{i\omega\rho}{\eta}}} \right], \tag{5}$$

where $i = \sqrt{-1}$. Equation (5) reduces to the stationary value of the dynamic permeability, $K_0 = \frac{b^2}{12}$, in the limit $\omega \to 0$.

Following the formalism described in Ref. [47] for a single sinusoidal mode of the form $F(t) = F_0 \cos(\omega t)$, the average velocity $\langle v \rangle$ in time domain can be written as

$$\langle v(t) \rangle = \frac{F_0}{\eta} [\mathrm{Re}\hat{K}(\omega) \cos(\omega t) + \mathrm{Im}\hat{K}(\omega) \sin(\omega t)], \tag{6}$$

which in turn can be expressed as

$$\langle v(t) \rangle = v_0(\omega) \cos(\omega t - \Phi), \tag{7}$$

where v_0, which we get from the numerical integrations as the amplitude of the periodic velocity, is given by $v_0 = \frac{F_0|K|}{\eta}$. Φ is the phase difference between the periodic force $F(t)$ and the velocity. In this way, the real and imaginary parts of the dynamic permeability can be written as

$$\mathrm{Re}\hat{K}(\omega) = \frac{v_0(\omega)\eta}{F_0} \cos(\Phi). \tag{8}$$

$$\mathrm{Im}\hat{K}(\omega) = \frac{v_0(\omega)\eta}{F_0} \sin(\Phi).$$

In order to use a similar framework for a binary fluid, we need to compute the dynamics of the velocity in both fluids. We introduce an effective viscosity, η_{eff}, given by

$$\eta_{\mathrm{eff}} = x_1\eta_1 + x_2\eta_2, \quad \text{where} \quad x_2 = L_2/L = 1 - x_1. \tag{9}$$

In what follows, we will consider two different expressions for the dynamic permeability: K_i^{phase}, useful to characterize each of the phases; and K^{channel}, useful to characterize the whole system.

K_i^{phase}, where $i = 1$ stands for the more viscous phase and $i = 2$ stands for the less viscous phase, is calculated with Eqs. (8) using the velocity $v_0 = v_i^{\mathrm{phase}}$, averaged over one of the two phases, as

$$v_i^{\mathrm{phase}} = \frac{1}{bL_i} \int_0^b \int_{L_i} v_z(y, z)\, dy\, dz, \tag{10}$$

and Φ, calculated as the phase difference between v_i^{phase} and the periodic force $F(t)$. K^{channel} is calculated with Eqs. (8) using the velocity $v_0 = v^{\mathrm{channel}}$, averaged over the whole channel, as

$$v^{\mathrm{channel}} = \frac{1}{bL} \int_0^b \int_L v_z(y, z)\, dy\, dz, \tag{11}$$

and Φ, calculated as the phase difference between v^{channel} and the periodic force $F(t)$.

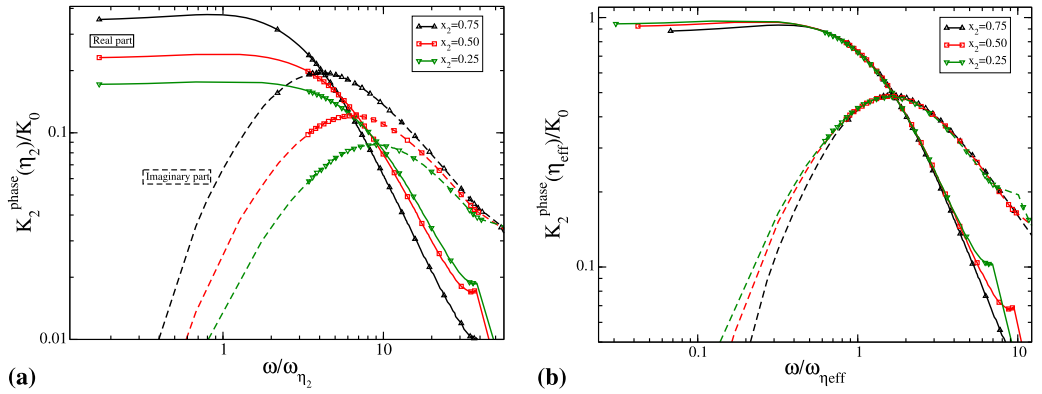

FIG. 2. Real part (full lines) and imaginary part (dashed lines) of the dynamic permeability K_2^{phase} of the less viscous phase. We have considered three different volume fractions: $x_2 = 0.25$, 0.5, and 0.75. The system size has been set as $L = 384$, $b = 22$, the viscosity of the outer phase has been set equal to $\eta_1 = 0.1$, and the viscosity contrast has been set equal to $\Delta\eta = 0.75$. The amplitude of the forcing was set as $F_0 = 3.55 \times 10^{-7}$. We have checked that the same results are obtained when halving or doubling the amplitude of the forcing, ensuring we work in the linear regime. (a) The permeability was calculated using the viscosity η_2 and the frequency was normalized by the viscous frequency ω_{η_2}. (b) The permeability was calculated using the effective viscosity η_{eff} and the frequency was normalized by the effective viscous frequency $\omega_{\eta_{\text{eff}}}$. In the Supplemental Material we show the deformation of the interface for $x_2 = 0.50$ and $\omega = \omega_{\eta_{\text{eff}}}/2$ [44].

We also define a non-dimensional viscosity contrast, as

$$\Delta\eta = \frac{\eta_1 - \eta_2}{\eta_1 + \eta_2}. \tag{12}$$

IV. RESULTS

Figure 2(a) shows the dynamic permeability, K_2^{phase}, in the lower viscosity phase as a function of the frequency of the driving force. The figure shows three curves, for three different systems, having different volume fractions x_2 of the low viscosity phase; the smaller the value of x_2, the smaller the size of the low-viscosity-phase slug. The dynamic permeability has been normalized by the steady state value for a single fluid, $K_0 = \frac{b^2}{12}$. The frequency has been normalized by the viscous frequency, $\omega_{\eta_2} = \frac{2\pi\eta_2}{\rho b^2}$. For each of the curves, that, as expected, are different, since they describe different systems, we observe the well-known behavior for a single fluid [28,48,49]; namely, at low frequencies, the fluid response is in phase with the driving force $F(t)$ (the imaginary part of the response has a value close to zero), and the real part of K_2^{phase} has a plateau, in a log-log scale. For larger frequencies, the real part decays and the imaginary part increases as a function of frequency. At frequencies larger than the frequency at which the real and the imaginary parts cross each other, the imaginary part also decays as a function of frequency. In the figure, we can see that the low frequency value of the permeability is specific to each value x_2; the larger the size of the low viscosity slug, the larger the value of the low frequency permeability. We have verified that, for a single fluid of viscosity η_2, the low frequency value of the normalized permeability is equal to 1. We also observe that the crossing frequency is specific to each value x_2. In addition, we observe a peak at frequencies close to $\omega/\omega_{\eta_2} \simeq 50$, whose precise location depends on x_2.

In Fig. 2(b) we show the same curves K_2^{phase}/K_0 using the effective viscosity introduced in Eq. (9), and a frequency normalized by the effective viscous frequency, $\omega_{\eta_{\text{eff}}} = \frac{2\pi\eta_{\text{eff}}}{\rho b^2}$. By doing so, we find a quasiuniversal curve that makes the permeability of the different systems coincide in a wide frequency range that includes the crossing frequency of the real and imaginary parts.

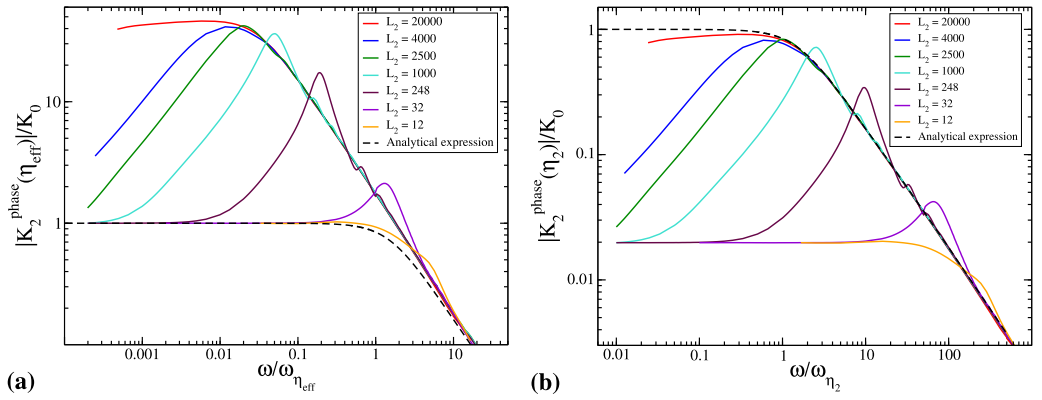

FIG. 3. Magnitude of the dynamic permeability of the less viscous phase, $|K_2^{\text{phase}}(\omega)|$. We have considered here different phase lengths L_2, with $\eta_1 = 1.0$, $\eta_2 = 10^{-2}$, and $x_1 = x_2 = 0.50$. The channel thickness has been set as $b = 10$. The amplitude of the forcing was set as $F_0 = 1.2 \times 10^{-6}$. We have checked that the same results are obtained when halving or doubling the amplitude of the forcing. (a) The permeability was calculated using the viscosity η_{eff} and the frequency was normalized by the viscous frequency $\omega_{\eta_{\text{eff}}}$. (b) The permeability was calculated using the effective viscosity η_2 and the frequency was normalized by the effective viscous frequency ω_{η_2}. The black dashed lines show the magnitude of the dynamic permeability given by the analytical expression in Eq. (5) for single fluids of viscosity η_{eff} (a) and η_2 (b).

The parameter $\omega/\omega_{\eta_{\text{eff}}}$ plays the role of a square Womersley number [50], adapted to the case of a binary fluid. Below the unit value of this number, there is a quasisteady behavior, for which the fluid velocity is practically in phase with the imposed forcing [51]. For large values of this number, the velocity is out of phase with the forcing.

For many fluidic systems, Fig. 2(b) provides a quasiuniversal curve for a binary fluid when the compressibility of the fluids is irrelevant; that is, when the frequency associated with compressible effects is much larger than the viscous frequency. However, this curve is quasiuniversal and not universal since the value of the dynamic permeability at low frequencies is slightly dependent on the value x_2, and the shoulder position at large frequencies depends of the volume fraction x_2. These details should not prevent us from appreciating that the framework of the dynamic permeability, originally developed for a single fluid, allows one to deeply simplify the dynamic description of a binary fluid, which is an otherwise very complex system, provided that it is made in terms of an effective viscosity and an associated effective viscous frequency. Figure 2(b) shows that in the regime where compressibility is irrelevant the scaling relation $K/K_0 = f(\omega/\omega_\eta)$ produces a universal behavior [48,49] for a binary fluid, only if the viscosity used in the calculation of K and ω_η is the effective viscosity given in Eq. (9). The parameters K_0 and $\omega_{\eta_{\text{eff}}}$ scale the real and imaginary parts of K not only in the low- and high-frequency limits, but also in the whole crossover region [28].

We now focus on a very different regime, where the compressibility of the low viscosity phase is relevant. For this regime, K_2^{phase} presents resonances. We found that a density contrast between the two phases is not necessary to observe resonances: all the results presented below hold in the presence or absence of a density contrast. We focus on the less viscous phase where the resonance can lead to a dramatic increase of the amplitude of fluid flow.

In Fig. 3 we consider the dynamic permeability K_2^{phase} in the case of a very strong viscosity contrast ($\eta_1 = 1.0$ and $\eta_2 = 10^{-2}$) for different lengths L_2, $b = 10$, and $x_1 = 0.50$. Figure 3(a) shows the dynamic permeability computed using the effective viscosity η_{eff}. For L_2 larger than 12, all of the curves present a maximum at a certain frequency which we call the resonance frequency. We clearly see that the position of the resonance frequency depends on the length L_2: the larger the

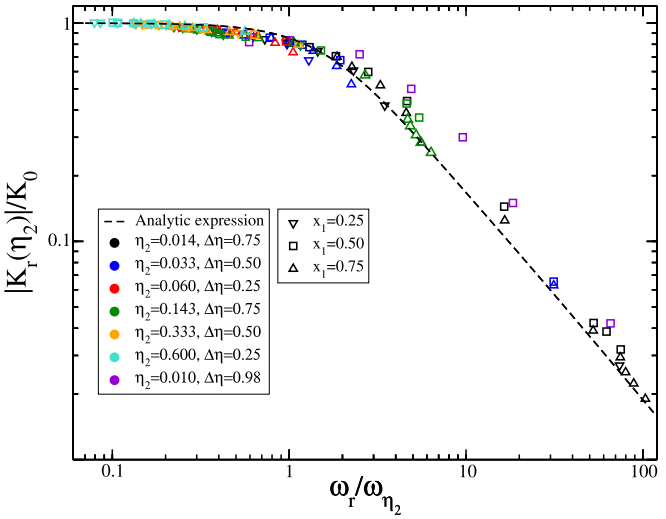

FIG. 4. Magnitude of the dynamic permeability at the resonance frequency $|K_r| = |K_2^{\text{phase}}(\eta_2, \omega_r)|$, computed from the viscosity in phase 2, as a function of ω_r/ω_{η_2}. We show here the results for all the values of b and L considered in the simulations. The black dashed line shows the magnitude of the dynamic permeability given by the analytical expression in Eq. (5) for a single fluid of viscosity η_2.

system size, the smaller the resonance frequency and the larger the magnitude of the permeability K_2^{phase} at resonance, $|K_r|$. In the case studied here, we reach values of $|K_r|$ up to 50 times the stationary value K_0 for L_2 larger than 2500. This means that flow amplitude at resonance is up to 50 times the steady state flow. For this regime, in which compressibility is relevant, η_{eff} does not make the curves collapse as when compressibility is irrelevant; in fact, a description in terms of η_2 allows for a clearer understanding of the underlying physics.

Figure 3(b) shows the dynamic permeability K_2^{phase} computed using the viscosity η_2 as a function of the driving frequency normalized by ω_{η_2}. For frequencies larger than the resonance frequency, or approximately equal to it, the dynamic behavior follows *grosso modo* the one of a single fluid of viscosity η_2, indicated by a black dashed line. This implies that the presence of the high viscosity fluid is not affecting the dynamics of the low viscosity one. In other words, at frequencies larger than the resonance frequency, the low viscosity fluid does not feel the resistance imposed by the high viscosity fluid. In fact, a plot of the permeability at resonance versus the resonance frequency follows closely the curve for a single fluid of viscosity η_2, particularly for values of $\omega_r/\omega_{\eta_2} < 1$, as shown in Fig. 4, for several viscosity contrasts and several system sizes.

Figure 5, for the dynamic permeability for the whole channel, $|K^{\text{channel}}|$, shows that the dynamics caused by the resonance of the low viscosity fluid is inherited by the average dynamics of the whole system. This implies that the compressibility of the low viscosity phase causes the binary fluid as a whole to have resonances at certain frequencies for which the amplitude of the velocity is maximum. In other words, the flow amplitude of a binary-fluid system in a zero-mean flow could be optimized if one chooses the driving frequency to be the one that puts the system at resonance.

V. ORIGIN OF RESONANCE

We now wish to study how the resonance frequency ω_r varies for different sets of viscosities and for different channel thicknesses, in terms of a dimensionless characteristic frequency of the system. One natural characteristic frequency of the system is the one at which standing waves are generated in an unconfined cavity, $\omega_{\text{comp}}^U = \pi c_s/L_2$ [52–54]. Another one is the viscous frequency ω_{η_2}, given

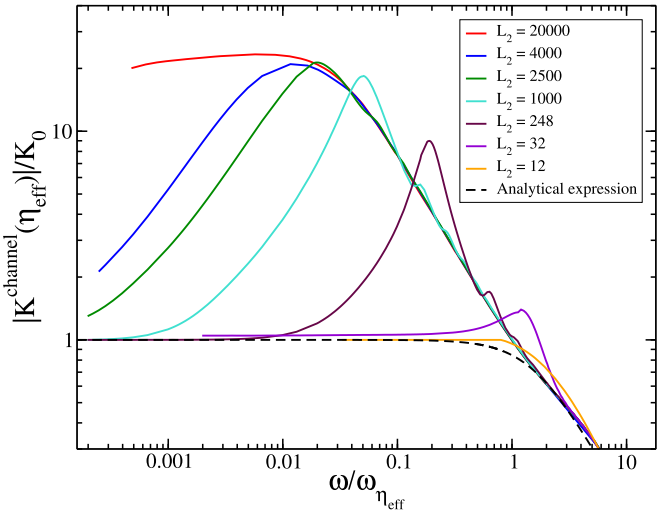

FIG. 5. Magnitude of the dynamic permeability of the whole channel, $|K^{\text{channel}}(\omega)|$. We have considered here different phase lengths L_2, with $\eta_1 = 1.0$, $\eta_2 = 10^{-2}$, and $x_1 = x_2 = 0.50$. The channel thickness has been set as $b = 10$. The amplitude of the forcing was set as $F_0 = 1.2 \times 10^{-6}$. The permeability was calculated using the viscosity η_{eff} and the frequency was normalized by the viscous frequency $\omega_{\eta_{\text{eff}}}$. The black dashed line shows the magnitude of the dynamic permeability given by the analytical expression in Eq. (5) for a single fluid of viscosity η_{eff}.

by the viscous resistance of phase 2. We therefore chose to use $\omega^U_{\text{comp}}/\omega_{\eta_2}$ as a nondimensional frequency to analyze our results. We expect two different regimes:

(i) The compressibility regime, $\omega^U_{\text{comp}}/\omega_{\eta_2} \gg 1$, in which the resonance should be controlled by the ability of the fluid to be compressed.

(ii) The viscous regime, $\omega^U_{\text{comp}}/\omega_{\eta_2} \ll 1$, in which the resonance should be controlled by the viscosity of phase 2.

Figure 6 shows, with symbols, the resonance frequency ω_r for different sets of viscosities (a) and for different channel thicknesses (b). We can clearly observe two distinct limiting regimes, at small and large values of the dimensionless frequency $\omega^U_{\text{comp}}/\omega_{\eta_2}$. In between these regimes, there is a crossover region where two phenomena compete to determine the exact location of the resonance. Note that in both regimes the compressibility effects are important, since they are causing the resonance to exist. So, the viscous regime should not be confused with the regime of Fig. 2, where the compressibility is irrelevant.

Figures 6(a) and 6(b) show that for very large values of $\omega^U_{\text{comp}}/\omega_{\eta_2}$ (above 100) we get the expected behavior $\omega_r/\omega^U_{\text{comp}} \approx 1$. However, for values of $\omega^U_{\text{comp}}/\omega_{\eta_2}$ below 100 we observe a deviation of the data towards lower resonant frequencies.

Confinement of a viscous fluid affects not only the damping of acoustic waves, but also their propagation velocity [55,56]. Based on Kirchhoff's expression [52,57], we can account for it by writing an effective sound velocity c_s', in terms of the sound velocity c_s, as $c_s' = c_s(1 - \alpha\sqrt{\frac{\omega_{\eta_2}}{\omega^U_{\text{comp}}}})$, where α is a coefficient that accounts for the confinement. With this, we can write a frequency at which standing waves are generated in a confined cavity, ω^C_{comp}, in terms of the one at which standing waves are generated in an unconfined cavity, as $\omega^C_{\text{comp}} = \pi c_s'/L_2 = \omega^U_{\text{comp}}(1 - \alpha\sqrt{\frac{\omega_{\eta_2}}{\omega^U_{\text{comp}}}})$. We have found that a value of $\alpha = 1/\sqrt{\pi}$ [58] gives a very good agreement with the simulations.

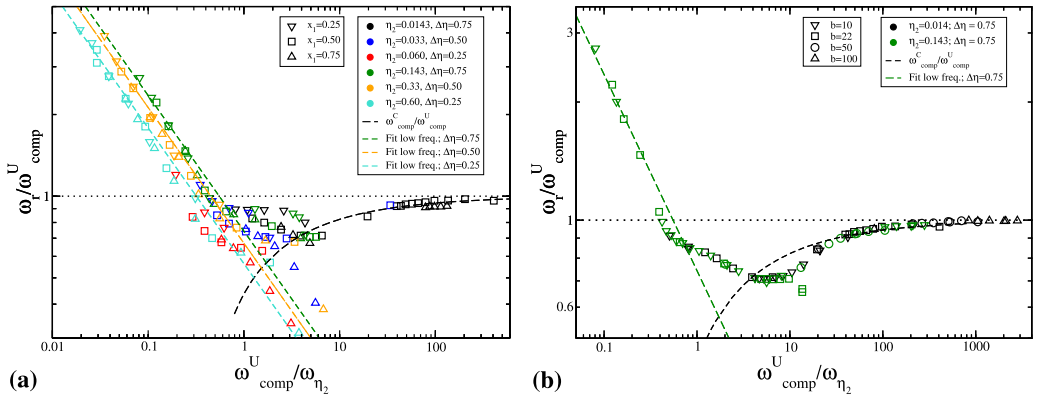

FIG. 6. $\omega_r/\omega^U_{\rm comp}$ as a function of $\omega^U_{\rm comp}/\omega_{\eta_2}$, where ω_{η_2} is the viscous frequency calculated in phase 2 and $\omega^U_{\rm comp} = \pi c_s/L_2$ is the frequency at which standing waves are generated in an unconfined cavity. (a) We consider a unique channel thickness $b = 22$. The symbols stand for the volume fractions and the colors for the viscosities of both phases. For each set of parameters x_2, η_1, and η_2 we consider a large range of lengths L. (b) We consider here $x_1 = 0.50$ and a constant viscosity contrast $\Delta\eta = 0.75$, and vary η_2 and b. For each set of b and η_2 we consider a large range of lengths L. The dashed lines show the results of the fits at large frequency [$\omega^C_{\rm comp}/\omega^U_{\rm comp}$, Eq. (13)] and low frequency ["Fit low frequency," Eq. (14)].

We therefore plot $\frac{\omega^C_{\rm comp}}{\omega^U_{\rm comp}}$ given by

$$\frac{\omega^C_{\rm comp}}{\omega^U_{\rm comp}} = 1 - \frac{1}{\sqrt{\pi}}\left(\frac{\omega^U_{\rm comp}}{\omega_{\eta_2}}\right)^{-\frac{1}{2}}. \tag{13}$$

with black dashed lines in Figs. 6(a) and 6(b). These curves show that the decrease in the value of the resonance frequency can be explained by the confinement of the fluid.

For the viscous regime ($\omega^U_{\rm comp}/\omega_{\eta_2} \ll 1$), Fig. 6(a) shows that the decay of $\omega_r/\omega^U_{\rm comp}$ follows a power law with a fixed exponent of $-1/2$, but with a prefactor dependent on the viscosity contrast. Figure 6(b) shows that varying the channel thickness does not change this power law. For low values of $\frac{\omega^U_{\rm comp}}{\omega_{\eta_2}}$ the expression

$$\frac{\omega_r}{\omega^U_{\rm comp}} = \Delta\eta^{\frac{1}{4}}\left(\frac{\pi\omega^U_{\rm comp}}{2\omega_{\eta_2}}\right)^{-1/2} \tag{14}$$

gives a very good agreement with the simulation results. This can be seen by looking at the three dashed straight lines in Fig. 6(a) and the dashed straight line in Fig. 6(b) plotted from Eq. (14). For a very large viscosity contrast, $\Delta\eta \simeq 1$, Eq. (14) gives $\omega_r/\omega^U_{\rm comp} = (\pi\omega^U_{\rm comp}/2\omega_{\eta_2})^{-1/2}$, which represents an upper bound for ω_r.

We have also found a universal curve on which all our simulation data fall, independently of the values of channel thickness, viscosities, and system lengths. This curve is obtained by introducing a new dimensionless frequency, given by the ratio of $\omega^C_{\rm comp}$ and a more complex frequency $\omega_{\rm int}$ involving the interplay of the viscous frequency, the frequency associated with unconfined compressibility and the viscosity contrast. The expression of $\omega_{\rm int}$ is given by:

$$\omega_{\rm int} = \Delta\eta^{1/4}\sqrt{\frac{2}{\pi}\omega^U_{\rm comp}\omega_{\eta_2}}. \tag{15}$$

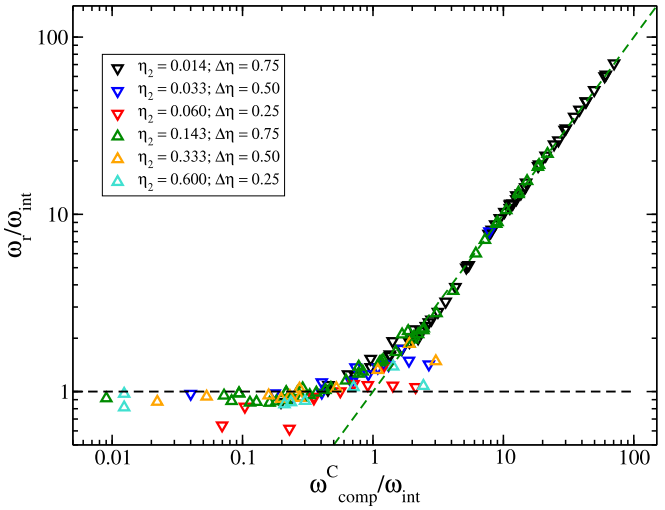

FIG. 7. $\omega_r/\omega_{\text{int}}$ as a function of $\omega^C_{\text{comp}}/\omega_{\text{int}}$ for different viscosity contrasts $\Delta\eta$. We show here, with symbols, the results obtained for all the sets of parameters used in our simulations, which include different values of b, L, and x_2. The dashed black line describes the resonant behavior in the viscous regime, $\omega_r = \omega_{\text{int}}$, while the dashed green line shows the resonant behavior in the compressibility regime, $\omega_r = \omega^C_{\text{comp}}$.

The universal curve can be seen in Fig. 7 where, in addition to the simulation results displayed with symbols, two dashed lines are plotted. These lines are given by $\frac{\omega_r}{\omega_{\text{int}}} = 1$ for the viscous regime and by $\frac{\omega_r}{\omega_{\text{int}}} = \frac{\omega^C_{\text{comp}}}{\omega_{\text{int}}}$ for the compressibility regime.

In conclusion, we find that the resonance frequency follows a universal curve that at low values of $\omega^C_{\text{comp}}/\omega_{\text{int}}$ is strongly dependent on the dynamic interaction between the two phases, and that at large values of $\omega^C_{\text{comp}}/\omega_{\text{int}}$ is dominated by the compressibility of the confined fluid.

VI. A GUIDE TO POTENTIAL EXPERIMENTS IN A STANDARD MICROFLUIDIC SETUP

In the first part of Sec. IV, we found that, for $\omega^C_{\text{comp}} \gg \omega_{\eta_{\text{eff}}}$, compressibility is irrelevant. We then proved that, when $\omega^C_{\text{comp}} < \omega_{\eta_{\text{eff}}}$, compressibility is relevant and generates resonances. We find that the transition between these two regimes depends on the more precise value of the nondimensional quantity $\omega^*_c = \omega^C_{\text{comp}}/3\omega_{\eta_{\text{eff}}}$.

In the second part of Sec IV, we found that the magnitude of the dynamic permeability at resonance, $|K_r|$, depends on the length L_2 for $\omega_r \geqslant \omega_{\eta_2}$. On the other hand, for $\omega_r < \omega_{\eta_2}$ the permeability at resonance $|K_r|$ is independent of the system length. Since in these regimes $\omega_r \simeq \omega_{\text{charac}}$, there is a nondimensional frequency $\omega^*_s = \omega_{\text{charac}}/\omega_{\eta_2}$ that characterizes the transition between the two resonant regimes. The expressions of these two nondimensional frequencies are

$$\omega^*_c = \frac{\omega^C_{\text{comp}}}{3\omega_{\eta_{\text{eff}}}} = \frac{\rho b^2 c_s}{6\eta_{\text{eff}} L_2}\left[1 - \sqrt{\frac{2\eta_2 L_2}{\pi \rho b^2 c_s}}\right],$$
$$\omega^*_s = \frac{\omega_{\text{charac}}}{\omega_{\eta_2}} = \Delta\eta^{1/4}\sqrt{\frac{\rho b^2 c_s}{\pi L_2 \eta_2}}. \tag{16}$$

Each of these expressions will give a value for the length, L_2, of the low viscosity slug: one for the transition between the regime where compressibility is relevant and the regime where it is irrelevant,

given by $L_c = L_2(\omega_c^* = 1)$, that is,

$$L_c = \frac{2\pi\rho b^2 c_s}{\eta_2\left[1+\sqrt{1+\frac{12\pi\eta_{\text{eff}}}{\eta_2}}\right]^2}; \tag{17}$$

and another one, within the compressibility regime, that indicates when the permeability at resonance, $|K_r|$, depends on L_2 and when it does not. This one is given by $L_s = L_2(\omega_s^* = 1)$, that is,

$$L_s = \frac{\rho b^2 c_s}{\pi\eta_2}\sqrt{\Delta\eta}. \tag{18}$$

In order to guide potential experiments, we report the values of L_c and L_s allowing $\omega_c^* = 1$ and $\omega_s^* = 1$ and the corresponding resonance frequencies, for two binary fluids:

(i) Water/air ($\rho_w = 1000$ kg/m^3, $\eta_w = 0.001$ Pa s, $\rho_a = 1$ kg/m^3, $\eta_a = 10^{-6}$ Pa s, $c_s = 350$ m/s, $\Delta\eta = 0.99$).

(ii) Mineral oil/bubbly water with a 0.1 volume ratio of air ($\rho_{\text{mo}} = 850$ kg/m^3, $\eta_{\text{mo}} = 0.03$ Pa s, $\rho_{bw} = 1000$ kg/m^3, $\eta_{bw} = 10^{-3}$ Pa s, $c_s = 50$ m/s, $\Delta\eta = 0.94$) [18,59–61].

We consider a microchannel of height $b = 55$ μm. We set the length of the more viscous slug to be $L_1 = 3$ cm. From Eqs. (17) and (18), we can now estimate the transition lengths and the corresponding characteristic frequencies [Eq. (16)].

For the water/air binary fluid, we find $L_c = 0.02$ cm and $L_s = 34$ cm. Compressibility is relevant for any value $L_2 > L_c$, and the resonance would be observed for driving frequencies $\omega < 9.85 \times 10^5$ Hz. The transition to a dynamic permeability at resonance, independently of the system size, would be reached for $L_2 > L_s$, which would lead to resonance frequencies $\omega_r < 330$ Hz. Considering the typical system lengths employed in microfluidics [62], only the regime for which the dynamic permeability at resonance depends on the system size would be observable for a water/air binary fluid. In these calculations we consider a purely isothermal situation, for which the correction to the sound velocity originates in the confinement of the fluid. In Appendix B, we give an expression for the frequency associated with compressibility of a confined fluid in an adiabatic situation; that leads to critical lengths and frequencies similar to the ones computed here.

For the mineral oil/bubbly water binary fluid, we find $L_c = 0.08$ cm and $L_s = 4.6$ cm. Compressibility is relevant for $L_2 > L_c$, and the resonance would be observed for driving frequencies $\omega < 2.9 \times 10^4$ Hz. The transition to a dynamic permeability at resonance, independently of the system size, could be reached for $L_2 > L_s$, which would lead to frequencies $\omega_r < 330$ Hz. For the mineral oil/bubbly water binary fluid, the two resonant regimes could, in principle, be experimentally observed.

For the two cases presented here, the onset for the relevance of compressibility, corresponds to very short lengths L_2 and very large frequencies. This implies that, for most of the systems involving a compressible fluid, the existence of the compressibility-induced resonance cannot be neglected.

VII. CONCLUSIONS

We have presented a complete description of the dynamic response of a binary fluid under a single-mode periodic forcing. For incompressible fluids or when the compressibility effects are negligible, namely when the frequency associated with the compressibility is larger than the effective viscous frequency, the dynamics of the binary fluid is equivalent to the one of a single fluid computed with an effective viscosity. In the opposite case, the ability of the less viscous fluid to be compressed allows for a resonance to arise. When this occurs, the low viscosity fluid behaves as if it were alone for driving frequencies $\omega \geqslant \omega_r$. We report the resonant frequency and magnitude of the dynamic permeability at resonance, as a function of the ratio of two parameters: the frequency associated with the compressibility, that accounts for confinement, and a more complex frequency, that involves both the viscous frequency and the frequency associated with the compressibility. The competition between these two characteristic frequencies gives rise to two regimes. In order to

guide potential experiments, we report at which system sizes and frequencies, within the actual capabilities of standard microfluidic experiments, our predictions could be confirmed, for two different binary fluids. Our calculations suggest that the onset of system sizes where compressibility is relevant is very small, implying that for most microfluidic devices the resonant behavior induced by compressibility has to be considered for a correct description of the dynamics.

ACKNOWLEDGMENTS

J.L. thanks DGAPA-UNAM for a two-year postdoctoral grant. I.P. acknowledges support from Ministerio de Ciencia, Innovación y Universidades (Grant No. PGC2018-098373-B-100) and from Generalitat de Catalunya under project 2017SGR-884, Swiss National Science Foundation Project No. 200021-175719. This work was partially funded by the Horizon 2020 program through 766972-FET-OPEN-NANOPHLOW. Part of the computational work herein was carried on in the MareNostrum Supercomputer at Barcelona Supercomputing Center. E.C.P. and J.L. acknowledge financial support from CONACyT (Mexico) through Project No. 219584 and from the Faculty of Chemistry, UNAM, through PAIP Project No. 5000-9011. E.C.P. acknowledges Professor Kerem Uguz and the Department of Chemical Engineering of Bogazici University for hosting her during a sabbatical leave.

APPENDIX A: DETAILS OF THE MODEL

To describe the two immiscible fluids, we introduce an order parameter ϕ that relates to the local variation of concentration between the two bulk phases. The free energy of the binary fluid $\mathcal{F}[\phi]$ is written as a functional of the local order parameter $\phi(\mathbf{r})$:

$$\mathcal{F}[\phi] = \int_V \left(W(\phi) + \frac{\epsilon}{2}(\vec{\nabla}\phi)^2 \right) dV + \int_S V_s(\phi_s)\, dS. \tag{A1}$$

$$W(\phi) = B\frac{\phi^4}{4} + A\frac{\phi^2}{2}, \tag{A2}$$

where we consider a thermodynamic contribution to the free energy via the double-well potential $W(\phi)$ and a square-gradient term that quantifies the energetic cost of the interface between the two phases. The second integral of Eq. (A1) controls the fluid-solid interaction [31]. In this paper we focus on the effect of the viscosity contrast and keep $V_s = 0$, which discards any preferential wetting of any of the two fluids and corresponds to a contact angle of 90°.

The order parameter varies between two extreme values corresponding to the bulk equilibrium concentrations at coexistence across an interfacial diffuse region. Those values are controlled by the parameters A, B, and ϵ. We consider the symmetric case $A = -B = -1$, which gives the equilibrium values $\phi_{\text{eq}} = \pm\sqrt{-A/B} = \pm 1$, the interface thickness $\xi = \sqrt{-\epsilon/2A}$, and the surface tension $\sqrt{-8\epsilon A^3/9B^2} = \sqrt{8\epsilon B/9}$. In all the simulations presented in this paper, the two phases are completely demixed; we deliberately chose an energy barrier large enough to assure so. We keep the surface tension $\sigma = 1.8 \times 10^{-4}$ and the interface thickness identical in all our simulations. We use $\xi = 2.83$, so that the interface spans over more than one lattice node.

From the expression of the free energy, we get the local chemical potential and pressure tensor:

$$\mu = \frac{\delta \mathcal{F}}{\delta \phi} = B\phi^3 + A\phi - \epsilon\nabla^2\phi. \tag{A3}$$

$$\Pi_{\alpha\beta} = \left[\frac{3}{4}B\phi^4 + \frac{1}{2}A\phi^2 - \epsilon\phi\nabla^2\phi - \frac{1}{2}\epsilon|\vec{\nabla}\phi|^2 \right]\delta_{\alpha\beta} + \epsilon(\partial_\alpha\phi)(\partial_\beta\phi). \tag{A4}$$

This leads to the equation for the advection and diffusion of the order parameter,

$$\frac{\partial\phi}{\partial t} + (\vec{v}\cdot\vec{\nabla})\phi = M\nabla^2\mu, \tag{A5}$$

and to the local force applied to the fluid due to the presence of the fluid-fluid interface,

$$F_\alpha^\phi = -\sum_\beta \partial_\beta \Pi_{\alpha\beta}. \tag{A6}$$

The contact line can move following the diffusive term in Eq. (A5). According to a large amount of literature [63–68] there is a solid basis that diffuse interface approaches lead to a realistic description of the motion of a contact line; such is the case of our diffuse interface model, for which the motion of the contact line can be controlled by the mobility parameter M.

As mentionned above, we use the lattice-Boltzmann method (LBM) to solve the dynamics of the system. To do so, we introduce a velocity distribution function f_i, the temporal evolution of which is described by the discretized Boltzman equation:

$$f_i(\vec{r}+\vec{c}_1, t+1) - f_i(\vec{r}, t) = -\frac{1}{\tau(\vec{r})}\left(f_i - f_i^{eq}\right) + F_i^t(\vec{c}_1, t). \tag{A7}$$

We use a discretization on space and time. The velocity vectors $\vec{c}_i$ join the different nodes of a cubic lattice. We consider a set of 19 velocity vectors in three dimensions, in the so-called D3Q19 model [69]. Equation (A7) is solved in two steps. During a collision step, described by the right-hand side of Eq. (A7), the distribution functions are relaxed to their equilibrium values while an external forcing is applied. The athermal LBM has long been shown to preserve satisfactorily the Galilean invariance [70–72] in the low Mach number limit (we use Mach numbers Ma < 0.1 in all the simulations). This property is also enforced by the multirelaxation time approach that we use to perform the collision step [73].

The periodic forcing is applied through a single-mode body force term $\vec{F}(t) = F_0 \cos(\omega t)\,\vec{e}_z$. This external body force adds to the local contribution from the binary fluid $\vec{F}^\phi$ [Eq. (A6)], which gives the distribution $F_i^t(t)$ when projected over the velocity set $\vec{c}_i$. We introduce a local dependence of the viscosity on the order parameter: $\eta(\vec{r}) = \eta_1 + \frac{\phi(\vec{r})-\phi_1}{\phi_2-\phi_1}(\eta_2-\eta_1)$ [39]. Then, the local relaxation time $\tau(\vec{r})$ is related to the local viscosity by $\eta(\vec{r}) = \rho c_s^2(\tau(\vec{r}) - \frac{1}{2})$. During a second step, each of the post-collision distribution functions f_i is advected in the direction of the associated velocity $\vec{c}_i$, as described in the left-hand side of Eq. (A7).

The hydrodynamic variables are recovered through the moments of the distribution functions f_i. The local density and momentum are given respectively by $\rho = \sum_i f_i$ and $\rho\vec{v} = \sum_i f_i\vec{c}_i$. The LBM intrinsically accounts for the fluid compressibility, which leads to an additional term in the equation of conservation of the momentum [Eq. (A9)] given by the gradient of the thermodynamic pressure $P_\rho = c_s^2\rho$, where ρ is the local fluid density and $c_s = 1/\sqrt{3}$ is the sound velocity.

Together with Eq. (A5), this gives a set of equations for the local dynamics of the fluid and order parameter out of equilibrium:

$$\frac{\partial\rho}{\partial t} + \vec{\nabla}\cdot(\rho\vec{v}) = 0. \tag{A8}$$

$$\rho\left(\frac{\partial\vec{v}}{\partial t} + (\vec{v}\cdot\vec{\nabla})\vec{v}\right) = -\vec{\nabla}\Pi - \vec{\nabla}P_\rho + \eta\nabla^2\vec{v} + \vec{F}(t). \tag{A9}$$

We consider a simulation box of dimensions $X \times b \times L$ in the x, y, and z directions respectively. We fix periodic boundary conditions on the x and z dimensions, which corresponds to a channel of width much larger than its thickness b. In all the simulations we take $X = 3$. The velocity profiles obey a no-slip and impenetrability condition set by $\vec{v}(y=0) = \vec{v}(y=b) = \vec{0}$. The no-slip and no-penetration boundary conditions at the solid boundaries are enforced using the bounce-back rules as described in Ref. [31].

APPENDIX B: EXPRESSION OF THE CHARACTERISTIC FREQUENCY ASSOCIATED WITH THE COMPRESSIBILITY OF THE FLUID IN ADIABATIC MOTION

The lattice-Boltzmann method we use is limited to purely isothermal situations, for which the resonance frequency in the regime dominated by compressibility can be described by $\omega_r = \omega^C_{\rm comp}$, with $\omega^C_{\rm comp} = \omega^U_{\rm comp}(1 - \frac{1}{\pi}\sqrt{\frac{\omega_{\eta_2}}{\omega^U_{\rm comp}}})$. Since we cannot consider adiabatic motion in our simulations, we can at least use an analytical expression in the literature to obtain a characteristic frequency of a confined fluid during an adiabatic process, $\omega^{CA}_{\rm comp}$, and estimate how much this value would change our predictions, as a guide to potential experiments. From the speed of sound reported in the literature [57], we can obtain

$$\omega^{CA}_{\rm comp} = \omega^U_{\rm comp}\left(1 - \frac{1}{\sqrt{\pi}}\sqrt{\frac{\omega_{\eta_2}}{\omega^U_{\rm comp}}} - \frac{1}{\sqrt{\pi}}\sqrt{\frac{\omega_{\rm adiab}}{\omega^U_{\rm comp}}}\right), \tag{B1}$$

where the characteristic adiabatic frequency $\omega_{\rm adiab}$ depends on the adiabatic index γ, the thermal conductivity κ, and the specific heat capacity C_v:

$$\omega_{\rm adiab} = 2\pi\frac{\kappa(\gamma-1)^2}{\gamma\rho C_v b^2}. \tag{B2}$$

We repeat the estimations of Sec. VI for the water/air binary mixture, using $\omega_{\rm adiab}$, with $\gamma = 1.4$, $\kappa = 0.026$ W/(m K) and $C_v = 718$ J/(kg K) (for air). We get $\omega_{\rm adiab} = 1368$ Hz, a value which is larger than $\omega_{\eta_2} = 330$ Hz. We found in Sec. VI that compressibility is relevant for any value $L_2 > L_c = 0.02$ cm and driving frequencies $\omega < 9.85 \times 10^5$ Hz. These values are almost identical when using $\omega^{CA}_{\rm comp}$ instead of $\omega^C_{\rm comp}$ in Eqs. (16) and (17): the relative change when taking into account the adiabatic correction is 2% on the value of L_c, and 0.01% on the value of the frequency at which the compressibility becomes relevant.

[1] K. Vijayakumar, S. Gulati, A. J. deMello, and J. B. Edel, Rapid cell extraction in aqueous two-phase microdroplet systems, Chem. Sci. **1**, 447 (2010).

[2] Q. Zhang, M. Zhang, L. Djeghlaf, J. Bataille, J. Gamby, A.-M. Haghiri-Gosnet, and A. Pallandre, Logic digital fluidic in miniaturized functional devices: Perspective to the next generation of microfluidic lab-on-chips, Electrophoresis **38**, 953 (2017).

[3] T. M. Squires and S. R. Quake, Microfluidics: Fluid physics at the nanoliter scale, Rev. Mod. Phys. **77**, 977 (2005).

[4] K. Jo, Y.-L. Chen, J. J. de Pablo, and D. C. Schwartz, Elongation and migration of single DNA molecules in microchannels using oscillatory shear flows, Lab. Chip **9**, 2348 (2009).

[5] M. R. Bringer, C. J. Gerdts, H. Song, J. D. Tice, and R. F. Ismagilov, Microfluidic systems for chemical kinetics that rely on chaotic mixing in droplets, Philos. Trans. R. Soc. London A **362**, 1087 (2004).

[6] J. Atencia and D. J. Beebe, Controlled microfluidic interfaces, Nature (London) **437**, 648 (2005).

[7] M. Srisa-Art, A. J. deMello, and J. B. Edel, High-throughput DNA droplet assays using picoliter reactor volumes, Anal. Chem. **79**, 6682 (2007).

[8] A. Huebner, S. Sharma, M. Srisa-Art, F. Hollfelder, J. B. Edel, and A. J. deMello, Microdroplets: A sea of applications? Lab. Chip **8**, 1244 (2008).

[9] M. Joanicot and A. Ajdari, Droplet control for microfluidics, Science **309**, 887 (2005).

[10] H. A. Stone, A. D. Stroock, and A. Ajdari, Engineering flows in small devices: Microfluidics toward a lab-on-a-chip, Annu. Rev. Fluid Mech. **36**, 381 (2004).

[11] H. Song, J. D. Tice, and R. F. Ismagilov, A microfluidic system for controlling reaction networks in time, Angew. Chem. Int. Ed. **42**, 768 (2003).

[12] A. Ochoa, E. Álvarez-Bohórquez, E. Castillero, and L. F. Olguín, Detection of enzyme inhibitors in crude natural extracts using droplet-based microfluidics coupled to HPLC, Anal. Chem. **89**, 4889 (2017).

[13] H. Song, D. L. Chen, and R. F. Ismagilov, Reactions in droplets in microfluidic channels, Angew. Chem. Int. Ed. **45**, 7336 (2006).
[14] K. Khoshmanesh, A. Almansouri, H. Albloushi, P. Yi, R. Soffe, and K. Kalantar-Zadeh, A multi-functional bubble-based microfluidic system, Sci. Rep. **5**, 9942 (2015).
[15] I. Glasgow and N. Aubry, Enhancement of microfluidic mixing using time pulsing, Lab. Chip **3**, 114 (2003).
[16] I. Glasgow, S. Lieber, and N. Aubry, Parameters influencing pulsed flow mixing in microchannels, Anal. Chem. **76**, 4825 (2004).
[17] Y. Xie, C. Chindam, N. Nama, S. Yang, M. Lu, Y. Zhao, J. D. Mai, F. Costanzo, and T. J. Huang, Exploring bubble oscillation and mass transfer enhancement in acoustic-assisted liquid-liquid extraction with a microfluidic device, Sci. Rep. **5**, 12572 (2015).
[18] P. A. Basilio, A. M. Torres Rojas, E. C. Poiré, and L. F. Olguín, Stream of droplets as an actuator for oscillatory flows in microfluidics, Microfluid. Nanofluid. **23**, 64 (2019).
[19] D. L. Johnson, J. Koplik, and R. Dashen, Theory of dynamic permeability and tortuosity in fluid-saturated porous media, J. Fluid Mech. **176**, 379 (1987).
[20] A. M. Chapman and J. J. L. Higdon, Oscillatory Stokes flow in periodic porous media, Phys. Fluids **4**, 2099 (1992).
[21] E. Corvera Poiré and A. Hernández-Machado, Frequency-induced stratification in viscoelastic microfluidics, Langmuir **26**, 15084 (2010).
[22] A. M. Torres Rojas, I. Pagonabarraga, and E. Corvera Poiré, Resonances of Newtonian fluids in elastomeric microtubes, Phys. Fluids **29**, 122003 (2017).
[23] J. Flores Gerónimo, A. Hernández-Machado, and E. Corvera Poiré, Enhanced imbibition from the cooperation between wetting and inertia via pulsatile forcing, Phys. Fluids **31**, 032107 (2019).
[24] M. Castro, M. E. Bravo-Gutiérrez, A. Hernández-Machado, and E. Corvera Poiré, Dynamic Characterization of Permeabilities and Flows in Microchannels, Phys. Rev. Lett. **101**, 224501 (2008).
[25] J.-L. Auriault, L. Borne, and R. Chambon, Dynamics of porous saturated media, checking of the generalized law of Darcy, J. Acoust. Soc. Am. **77**, 1641 (1985).
[26] T. Cubaud and C.-M. Ho, Transport of bubbles in square microchannels, Phys. Fluids **16**, 4575 (2004).
[27] P. S. Wilson and R. A. Roy, An audible demonstration of the speed of sound in bubbly liquids, Am. J. Phys. **76**, 975 (2008).
[28] E. Charlaix, A. P. Kushnick, and J. P. Stokes, Experimental Study of Dynamic Permeability in Porous Media, Phys. Rev. Lett. **61**, 1595 (1988).
[29] S. Vedel, L. Højgaard Olesen, and H. Bruus, Pulsatile microfluidics as an analytical tool for determining the dynamic characteristics of microfluidic systems, J. Micromech. Microeng. **20**, 035026 (2010).
[30] A. Hashmi, G. Yu, M. Reilly-Collette, G. Heiman, and J. Xu, Oscillating bubbles: A versatile tool for lab on a chip applications, Lab. Chip **12**, 4216 (2012).
[31] J.-C. Desplat, I. Pagonabarraga, and Peter Bladon, LUDWIG: A parallel Lattice-Boltzmann code for complex fluids, Comput. Phys. Commun. **134**, 273 (2001).
[32] Y. Q. Zu and S. He, Phase-field-based lattice Boltzmann model for incompressible binary fluid systems with density and viscosity contrasts, Phys. Rev. E **87**, 043301 (2013).
[33] C.-H. Shih, C.-L. Wu, L.-C. Chang, and C.-A. Lin, Lattice Boltzmann simulations of incompressible liquid-gas systems on partial wetting surfaces, Philos. Trans. R. Soc. London A **369**, 2510 (2011).
[34] J. Tölke, M. Krafczyk, M. Schulz, and E. Rank, Lattice Boltzmann simulations of binary fluid flow through porous media, Philos. Trans. R. Soc. London A **360**, 535 (2002).
[35] A. Pazdniakou and P. M. Adler, Dynamic permeability of porous media by the lattice Boltzmann method, Adv. Water Resour. **62**, 292 (2013).
[36] G. E. Pavlovskaya, T. Meersmann, C. Jin, and S. P. Rigby, Fluid flow in a porous medium with transverse permeability discontinuity, Phys. Rev. Fluids **3**, 044102 (2018).
[37] R. Teshigawara and A. Onuki, Spreading with evaporation and condensation in one-component fluids, Phys. Rev. E **82**, 021603 (2010).
[38] M. E. Cates and E. Tjhung, Theories of binary fluid mixtures: From phase-separation kinetics to active emulsions, J. Fluid Mech. **836**, P1 (2018).

[39] J. Chin, E. S. Boek, and P. V. Covene, Lattice Boltzmann simulation of the flow of binary immiscible fluids with different viscosities using the Shan-Chen microscopic interaction model, Philos. Trans. R. Soc. London A **360**, 547 (2002).
[40] B. M. Mognetti and J. M. Yeomans, Modeling receding contact lines on superhydrophobic surfaces, Langmuir **26**, 18162 (2010).
[41] R. Ledesma-Aguilar, D. Vella, and J. M. Yeomans, Lattice-Boltzmann simulations of droplet evaporation, Soft Matter **10**, 8267 (2014).
[42] A. M. J. Edwards, R. Ledesma-Aguilar, M. I. Newton, C. V. Brown, and G. McHale, Not spreading in reverse: The dewetting of a liquid film into a single drop, Sci. Adv. **2**, e1600183 (2016).
[43] R. Ledesma-Aguilar, I. Pagonabarraga, and A. Hernández-Machado, Three-dimensional aspects of fluid flows in channels. I. Meniscus and thin film regimes, Phys. Fluids **19**, 102112 (2007).
[44] See Supplemental Material at http://link.aps.org/supplemental/10.1103/PhysRevFluids.5.064201 for a video of the interface deformation, for $L = 384$, $b = 22$, $x_2 = 0.5$, $\eta_1 = 0.1$, $\Delta\eta = 0.75$, $F_0 = 3.5510^{-7}$ and $\omega = \omega_{\eta_{\text{eff}}}/2$.
[45] M. A. Knackstedt, M. Sahimi, and D. Y. C. Chan, Cellular-Automata calculation of frequency-dependent permeability of porous media, Phys. Rev. E **47**, 2593 (1993).
[46] M. E. Bravo-Gutierrez, M. Castro, A. Hernández-Machado, and E. Corvera Poiré Controlling viscoelastic flow in microchannels with slip, Langmuir **27**, 2075 (2011).
[47] R. Collepardo-Guevara and E. Corvera Poiré, Controlling viscoelastic flow by tuning frequency during occlusions, Phys. Rev. E **76**, 026301 (2007).
[48] P. Sheng and M.-Y. Zhou, Dynamic Permeability in Porous Media, Phys. Rev. Lett. **61**, 1591 (1988).
[49] M.-Y. Zhou and P. Sheng, First-principles calculations of dynamic permeability in porous media, Phys. Rev. B **39**, 12027 (1989).
[50] J. R. Womersley, Method for the calculation of velocity, rate of flow and viscous drag in arteries when the pressure gradient is known, J. Physiol. **127**, 553 (1955).
[51] C. Loudon and A. Tordesillas, The use of the dimensionless Womersley number to characterize the unsteady nature of internal flow, J. Theor. Biol. **191**, 63 (1998).
[52] D. B. Cruikshank, Experimental investigation of finite-amplitude acoustic oscillations in a closed tube, J. Acoust. Soc. Am. **52**, 1024 (1972).
[53] G. King, *Vibrations and Waves* (Wiley, New York, 2009).
[54] Y. A. Ilinskii, B. Lipkens, T. S. Lucas, T. W. Van Doren, and E. A. Zabolotskaya, Nonlinear standing waves in an acoustical resonator, J. Acoust. Soc. Am. **104**, 2664 (1998).
[55] G. P. Ward, R. K. Lovelock, A. R. J. Murray, A. P. Hibbins, and J. R. Sambles, Boundary-Layer Effects on Acoustic Transmission Through Narrow Slit Cavities, Phys. Rev. Lett. **115**, 044302 (2015).
[56] M. N. Mikhail and M. R. El-Tantawy, The acoustic boundary layers: A detailed analysis, J. Comput. Appl. Math. **51**, 15 (1994).
[57] D. E. Weston, The theory of the propagation of plane sound waves in tubes, Proc. Phys. Soc. London, Sect. B **66**, 695 (1953).
[58] A value $\alpha = 1/\sqrt{4\pi}$ is given in Ref. [57] in the case of a cylindrical channel.
[59] S. G. Kargl, Effective medium approach to linear acoustics in bubbly liquids, J. Acoust. Soc. Am. **111**, 168 (2002).
[60] C. Xie and J. P. Hartnett, Influence of variable viscosity of mineral oil on laminar heat transfer in a rectangular duct, Int. J. Heat Mass Transf. **35**, 641 (1992).
[61] H. S. Ju, E. J. Gottlieb, D. R. Augenstein, G. J. Brown, and B. R. Tittmann, An empirical method to estimate the viscosity of mineral oil by means of ultrasonic attenuation, IEEE Trans. Ultrason. Ferroelectr. Freq. Control **57**, 1612 (2010).
[62] P. Vázquez-Vergara, A. M. Torres Rojas, P. E. Guevara-Pantoja, E. Corvera Poiré, and G. A. Caballero-Robledo, Microfluidic flow spectrometer, J. Micromech. Microeng. **27**, 077001 (2017).
[63] M. Latva-Kokko and D. H. Rothman, Scaling of Dynamic Contact Angles in a Lattice-Boltzmann Model, Phys. Rev. Lett. **98**, 254503 (2007).
[64] A. J. Briant and J. M. Yeomans, Lattice Boltzmann simulations of contact line motion. II. Binary fluids, Phys. Rev. E **69**, 031603 (2004).

[65] R. Ledesma-Aguilar, R. Nistal, A. Hernandez-Machado, and I. Pagonabarraga, Controlled drop emission by wetting properties in driven liquid filaments, Nat. Mater. **10**, 367 (2011).
[66] R. Ledesma-Aguilar, A. Hernandez-Machado, and I. Pagonabarraga, Theory of Wetting-Induced Fluid Entrainment by Advancing Contact Lines on Dry Surfaces, Phys. Rev. Lett. **110**, 264502 (2013).
[67] H. Kusumaatmaja, E. J. Hemingway, and S. M. Fielding, Moving contact line dynamics: From diffuse to sharp interfaces, J. Fluid Mech. **788**, 209 (2016).
[68] C. M. Pooley, H. Kusumaatmaja, and J. M. Yeomans, Contact line dynamics in binary lattice Boltzmann simulations, Phys. Rev. E **78**, 056709 (2008).
[69] V. M. Kendon, M. E. Cates, I. Pagonabarraga, J. C. Desplat, and P. Bladon, Inertial effects in three-dimensional spinodal decomposition of a symmetric binary mixture: A Lattice-Boltzmann study, J. Fluid Mech. **440**, 147 (2001).
[70] Y. H. Qian, D. D'Humieres, and P. Lalemand, Lattice BGK models for Navier-Stokes equation, Europhys. Lett. **17**, 479 (1992).
[71] H. Chen, S. Chen, and W. H. Matthaeus, Recovery of the Navier-Stokes equations using a lattice-gas Boltzmann method, Phys. Rev. A **45**, R5339 (1992).
[72] X. B. Nie, X. Shan, and H. Chen, Galilean invariance of lattice Boltzmann models, Europhys. Lett. **81**, 34005 (2008).
[73] S. Succi, *The Lattice Boltzmann Equation For Complex States of Flowing Matter* (Oxford University Press, Oxford, 2018), Chap. 14.